Experimental studies of g-ratio MRI in ex vivo mouse brain[☆]

Kathryn L. West[a,b], Nathaniel D. Kelm[a,b], Robert P. Carson[c,d], Daniel C. Alexander[e], Daniel F. Gochberg[f,b], Mark D. Does[a,b,f,g,*]

[a]*Department of Biomedical Engineering, Vanderbilt University, Nashville, TN, US*
[b]*Institute of Imaging Science, Vanderbilt University Medical Center, Nashville, TN, US*
[c]*Department of Pediatrics, Vanderbilt University Medical Center, Nashville, TN, US*
[d]*Department of Neurology, Vanderbilt University Medical Center, Nashville, TN, US*
[e]*Center for Medical Image Computing, Department of Computer Science, University College London, London, United Kingdom*
[f]*Department of Radiology and Radiological Sciences, Vanderbilt University Medical Center, Nashville, TN, US*
[g]*Department of Electrical Engineering, Vanderbilt University, Nashville, TN, US*

Abstract

This study aimed to experimentally evaluate a previously proposed MRI method for mapping axonal g-ratio (ratio of axon diameters, measured to the inner and outer boundary of myelin). MRI and electron microscopy were used to study excised and fixed brains of control mice and three mouse models of abnormal white matter. The results showed that g-ratio measured with MRI correlated with histological measures of myelinated axon g-ratio, but with a bias that is likely due to the presence of non-myelinated axons. The results also pointed to cases where the MRI g-ratio model simplifies to be primarily a function of total myelin content.

Keywords: MRI, myelin, g-ratio, relaxometry, diffusion, microstructure.

1. Introduction

Myelin is a key component of healthy white matter, necessary for efficient action potential conduction along axons. Changes in myelin content and structure occur in several neurodegenerative diseases, such as Multiple Sclerosis (MS) (Lassmann, 2004) and Alzheimer's disease (Bartzokis, 2004). Additionally, abnormal axon and myelin development cause altered connectivity that may be a key factor in neuropsychiatric disorders such as Autism Spectrum Disorder (Weinstein et al., 2011),

[☆]Grant Sponsor: NIH EB001744, NIH EB019980, NSF GRFP DGE-0909667, NIH S10 RR029523, NIH 5K08 NS050484

[*]Corresponding author
Email address: mark.does@vanderbilt.edu (Mark D. Does)

Schizophrenia (Mighdoll et al., 2015), and Obsessive Compulsive Disorder (Menzies et al., 2008). Various MRI methods aim to report on the amount of myelin per imaging voxel (Laule et al., 2006, 2007; Alonso-Ortiz et al., 2015; West et al., 2016b), but a measure that reports on the relative myelin to axon volumes may provide a more sensitive and functionally specific evaluation of pathology. The g-ratio of myelinated axons—the ratio of axon diameters to the inner and outer boundaries of myelin—is one such measure that is thought to reflect a physiological optimization of axonal function (Chomiak and Hu, 2009; Rushton, 1951).

The only validated technique to measure the g-ratio is electron microscopy, which allows direct visualization of myelinated axons in cross section. However, this approach is slow, expensive, limited to ex vivo analysis, and not suitable for whole brain analysis. To move beyond the limitations of electron microscopy and extend g-ratio measurements into the MRI domain, Stikov et al. proposed a geometric model that relates myelin, axon, and extra-axon volume fractions (defined here as f_M, f_A, and f_E, respectively) to an aggregate g-ratio index, referred to here as g_{MRI}, (Stikov et al., 2011, 2015). With $f_A + f_E + f_M = 1$, any two volume fractions can be used to compute g_{MRI}, such as,

$$g_{MRI} = \frac{1}{\sqrt{1 + f_M/f_A}}. \tag{1}$$

This model assumes a constant g-ratio of all axons within a voxel, but West et al. later showed that g_{MRI} is equal to the square-root of the axon-area weighted mean of g^2 values from all axons in the voxel (West et al., 2016a). To date, a few combinations of MRI methods for measuring f_M and f_A have been used for g_{MRI} (Berman et al., 2016; Campbell et al., 2017; Dean et al., 2016; Mancini et al., 2017; Mohammadi et al., 2015; Stikov et al., 2011, 2015) but only one study, involving a single, normal macaque brain, has compared g_{MRI} data to g-ratio measurements from histology (Stikov et al., 2015).

The present study aimed to fill this gap in experimental work and specifically to evaluate g_{MRI} as a tool for ex vivo analysis of whole mouse brain. To this end, we analyzed previously-acquired MRI and electron microscopy data from 15 mouse brains, including 3 each from 3 different knockout models that exhibit abnormal myelination. Myelin content was measured using multi-exponential T_2 (MET_2) analysis, as recently evaluated in the same mouse models (West et al., 2016b), and axon content was probed using 2-shell diffusion weighted MRI (DWI) and three different analysis methods. Combinations of these measures were used to make a series of g_{MRI} maps, which were then quantitatively compared to histological measures of g-ratio.

2. Methods

Most of the experimental methods, including tissue preparation, data acquisition (MRI and electron microcopy) and much of the analysis, have been previously reported in detail (Kaden et al., 2016a; Kelm et al., 2016; West et al., 2016b), and are briefly summarized below.

2.1. Tissue Preparation

The Vanderbilt University Institutional Animal Care and Use Committee approved all animal studies. The brains of 15 adult mice were perfusion-fixed (2.5% glutaraldehyde + 2% paraformaldehyde), washed of fixative, and loaded (during and following perfusion) with 1.0 mM Gd-DTPA (Magnevist; Berlex, Montville, NJ). The 15 mice included control animals (n = 6) along with two conditional knockout (CKO) models of hypomyelination and one of hypermyelination (n = 3 for each model). In the first model, the *Tsc2* gene was deleted (*Tsc2 Olig2-Cre CKO*, conditional knockout), resulting in an extreme loss of myelinated axons (Carson et al., 2015). The second model targets *Rictor* (*Rictor Olig2-Cre CKO*), a key component of the mTORC2 complex, and also displays hypomyelination, but less severe than the *Tsc2* model. Previously reported similar models (*Tsc1 Emx1-Cre* and *Rictor Emx1-Cre*) showed similar hypomyelination (Carson et al., 2012, 2013). The third model results from the deletion of *Pten* (*Pten Olig2-Cre CKO*) leading to activation of the PI3K/Akt signaling pathway and subsequent hypermyelination (Harrington et al., 2010).

2.2. MRI Acquisition

All imaging was performed on a 15.2-T 11-cm horizontal bore Bruker (Rheinstetten, Germany) BioSpec scanner, using a 35-mm diameter Bruker quadrature volume coil for transmission and reception. To provide a signal-free background and prevent tissue dehydration, brains were placed in an MR-compatible tube filled with perfluoropolyether liquid (Fomblin, Solvay Solexis, Thorofarem NJ, USA). Scans were encoded with a matrix size of 128 × 96 × 72 over a 1.92 × 1.44 × 1.08 cm^3 FOV, resulting in 150 μm isotropic resolution.

For MET_2 imaging, a 3D multiple spin-echo sequence was used with non-selective excitation and refocusing pulses. Scan parameters were: repetition time (TR) = 520 ms, first echo time (TE) and echo spacing (ESP) = 5.8 ms, echo train length (ETL) = 18, receiver bandwidth = 38.5 kHz, and number of averaged excitations = 6. Total scan time was ≈ 6 hr. Diffusion weighted images were acquired using a 3D diffusion weighted fast spin echo sequence with TR/TE/ESP = 200/19.0/7.1 ms and ETL = 4 (Beaulieu et al., 1993; Kelm et al., 2016). Diffusion weighting was achieved with gradient pulse duration (δ) = 5 ms, diffusion time (Δ) = 12 ms,

prescribed b-values = 3000 and 6000 s/mm^2, 30 directions (Jones et al., 1999), 2 averaged excitations with gradient polarity reversal to mitigate background gradient cross-terms, and five b=0 images. The total scan time was ≈ 12 hr.

2.3. MRI Data Analysis

All data analysis was performed using MATLAB (R2014a-R2017a, The Mathworks, Natick MA) or Python 2.7.6, and MET$_2$ analyses were performed using the freely available Multi Exponential Relaxation Analysis (MERA) toolbox (Does, 2014) for MATLAB. Prior to Fourier reconstruction, k-space data for all images were apodized using a 3D Tukey window with a 0.25 taper-to-window ratio and zero-padded 2×, resulting in 75 μm nominal isotropic resolution.

For MET$_2$ analysis, the T_2 spectrum was estimated voxelwise using a linear inverse approach (Whittall and MacKay, 1989) by fitting the spin echo magnitudes to the sum of 100 extended-phase-graph-defined signals (Hennig, 1988) with T_2 values logarithmically spaced between TE/2 and 500 ms, similar to previous work (Prasloski et al., 2012; West et al., 2016b). From each spectrum, the myelin water fraction (MWF) was defined as the fraction of signal components with mean-T_2 < 17 ms (West et al., 2016b).

The three DWI data analyses each provided an estimate of the fraction of DWI signal (i.e., excluding myelin signal) resulting from axonal water, called the axon water fraction (AWF). Thus, in our three compartment model, AWF = $f_A/(f_A + f_E)$ and $f_A = (1 - f_M)$AWF. Method 1: the neurite orientation dispersion and density imaging (NODDI) model (Zhang et al., 2012) was implemented using the AMICO software (Daducci et al., 2015). The fixed model parameters d_{iso} (diffusion coefficient of the isotropically diffusing compartment) and $d_\parallel$ (unrestricted diffusion coefficient in the intra- and extra-axonal compartments) were set to 2 μm^2/ms and 0.35 μm^2/ms, respectively. (A range of $d_\parallel$ were tested and this one resulted in the strongest correlations of g-ratio measurements between MRI and histology.) Then, using standard NODDI notation, AWF = $v_{ic}(1 - v_{iso})$, where v_{ic} and v_{iso} are volumes of intra-cellular and isotropically-diffusion water, respectively.

Method 2: the multi-compartment spherical mean (mcSMT) analysis (Kaden et al., 2016a,b) involved computing the mean of the 30 diffusion-weighted signal magnitudes (i.e., the spherical mean) for each b-value, which factored out the effects of crossing fibers and orientation dispersion. The resulting 3-element signal vector was then modeled as the sum of signals from intra- and extra-neurite water compartments, as described previously (Kaden et al., 2016a). Here, the AWF is equal to signal fraction from the intra-neurite component. Method 3: the kurtosis tensor (Jensen and Helpern, 2010) was estimated using a constrained linear least-squares approach (Tabesh et al., 2011) and then the white matter tract integrity (WMTI) model (Fieremans et al., 2011) provided an estimate of AWF as AWF = $K_{max}/(K_{max} + 3)$, where K_{max} is the maximum kurtosis over all directions.

All parameter maps (MWF, and AWF from each DWI analysis method) for a given mouse were co-registered to an arbitrarily chosen reference brain using a combination of rigid affine registration followed by a non-rigid deformable demons registration (Thirion, 1998). The registered MWF maps were converted to myelin volume fraction maps using

$$f_{\mathrm{M}} = \frac{MWF \times \Phi_{\mathrm{H_2O,NM}}}{MWF \times \left(\Phi_{\mathrm{H_2O,NM}} - \Phi_{\mathrm{H_2O,M}}\right) + \Phi_{\mathrm{H_2O,M}}}, \tag{2}$$

where $\Phi_{\mathrm{H_2O,M}}$ and $\Phi_{\mathrm{H_2O,NM}}$ are the water proton pool volume fractions in myelin and non-myelin white matter, respectively (West et al., 2016b). The registered AWF maps were each scaled by $(1 - f_{\mathrm{M}})$ to generate f_{A} maps for each DWI analysis method.

From here, Eq (1) was used to generate g_{MRI} maps for every different DWI analysis method. For comparison, g_{MRI} maps were also computed using a simplified model that did not require estimates of f_{A}: assuming zero extra-axonal volume fraction, Eq (1) reduces to $g_{\mathrm{MRI}}\big|_{f_{\mathrm{E}}=0} = \sqrt{1 - f_{\mathrm{M}}}$. Finally, from a mid-sagittal slice, four white matter ROIs—the genu (GCC), mid-body (MCC), splenium (SCC) of the corpus callosum, and anterior commissure (AC)—were manually defined, and the mean value of each g_{MRI} measures was tabulated for each ROI and brain.

2.4. Microscopy

After MRI acquisition, from each brain a 1-2 mm thick sagittal section of tissue was cut from the left hemisphere beginning at the inter-hemispheric boundary, and 4 sub-regions corresponding to the 4 ROIs were prepared for ultra-thin sectioning and electron microscopy. Microscopic images were collected using a Philips/FEI Tecnai T12 electron microscope (FEI Company, Hillsboro, OR). For quantification of myelinated axon microstructure, 6-12 15,000× images were acquired per ROI and animal. These images contained a total of $N_{\mathrm{A}} \approx 350, 300, 250, 100$ myelinated axons (per ROI and animal) for control, *Rictor*, *Pten*, *Tsc2* mice, respectively.

Each image was analyzed semi-automatically, which provided segmentation of each myelinated axon and surrounding myelin, as previously described (West et al., 2016b). Measures of area (a_i) and myelin thickness (ϵ_i) were computed for the ith myelinated axon, $i = 1$ to N_{A}. Using a circular axon model, the g-ratio per myelinated axon was computed as $g_i = \sqrt{a_i} \big/ \left(\epsilon_i \sqrt{\pi} + \sqrt{a_i}\right)$. For comparison to g_{MRI} measures, the histological measure of g-ratio was defined as the root area-weighted mean square value of per-axon g (West et al., 2016a),

$$g_{\mathrm{HIST}} \triangleq \sqrt{\sum_{i=1}^{N_{\mathrm{A}}} a_i g_i^2 \Big/ \sum_{i=1}^{N_{\mathrm{A}}} a_i}, \tag{3}$$

and was computed for each ROI and brain. Because the non-myelinated axons were not segmented from this analysis, it was not possible to compute histological measures of f_A or f_E (or, consequently, AWF).

3. Results

Example raw and processed histology data are shown in Fig 1. On the top are raw images from the MCC of each of the four different types of mice, in the middle are the corresponding images after segmentation and analysis to determine per-axon measures of g-ratio, and on the bottom are histograms of g-ratio values from all the microscopy images for that brain and ROI. (Note the difference between g_{HIST} values, which are area-weighted, and the algebraic means.) A summary of the means and standard deviations of g_{HIST} values from each ROI and mouse type is shown in Fig 2. For comparison to literature, the algebraic mean g-ratio across all control mice and ROIs was 0.72 ± 0.018. This value is slightly lower than previous predictions for rat brain (0.77) (Chomiak and Hu, 2009) or experimental evaluations from mouse corpus callosa (0.76-0.81) (Arnett et al., 2001; Mason et al., 2001). These lower g-ratio values may reflect a systematic overestimation of myelin thickness resulting from the semiautomated segmentation. As expected though, the *Tsc2* mice exhibited a substantial loss of myelinated axons while the *Rictor* and *Pten* mice differed from controls primarily by having thinner and thicker myelin, respectively. Compared to the control mice, g_{HIST} was generally greater for the *Rictor* and *Tsc2* mice and lower for the *Pten* mice. Note that these histology derived measures of g-ratio did not include analysis of non-myelinated axons, which were apparent in all mice and especially abundant in the *Tsc2* mice.

The MRI measures of f_M have been previously reported and evaluated in comparison to histology, (West et al., 2016b). Briefly, this study showed $f_M \approx 0.05$, 0.15, 0.20, and 0.25, for *Tsc2*, *Rictor*, control, and *Pten* mice, respectively, and a strong and accurate linear correlation with histological measures of myelin volume ($r^2 = 0.68$). The various DWI derived measures of AWF are shown in Fig 3; however, without a gold-standard measure of AWF from histology, the accuracies of these different methods could be not be quantitatively evaluated. A qualitative evaluation of the histology indicated that across mouse types and ROIs, most of the space between the segmented myelinated axons was filled with non-myelinated axons or other cellular space (see Fig 1), which is most consistent with the relatively high AWF values resulting from mcSMT analysis, and the relatively invariant measures of AWF from both the mcSMT and WMTI analyses.

Representative g_{MRI} maps of each mouse model and DWI analysis method are shown in Fig 4. (For reference, supplementary Fig S1 shows example f_M and f_A maps.) These g_{MRI} maps were generated for voxels with f_M values > 0.01 and fractional anisotropy > 0.25 in the control brain shown, and are overlaid on greyscale

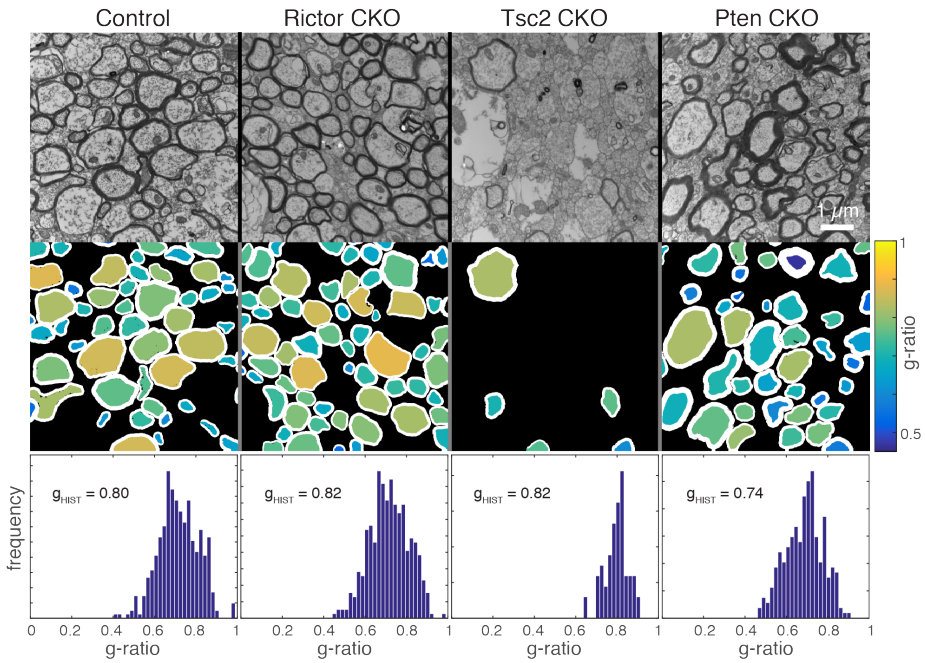

Figure 1: (top) Representative electron microscopy from the MCC of four different mice, one of each type. (middle) The same images after segmentation, with each axon's fill-color defined by its g-ratio. (bottom) Histograms of g-ratio values of all MCC axons measured from the individual mice corresponding to the histology above. For reference, the g_{HIST} value is shown for each histogram, and the corresponding algebraic mean g-ratios are 0.72, 0.72, 0.80, and 0.69. For ease of comparison, each histogram has been scaled to have the same peak amplitude.

$b = 0$ images from the DWI acquisition. Consistent with histology results, these maps show, compared to control mice, relatively higher g-ratio values in *Rictor* and *Tsc2* mice and lower values in the *Pten* mice.

Across all brains and ROIs, Fig 5 shows scatter plots and linear correlations of each g_{MRI} measure with g_{HIST}. In all cases, the linear correlations are statistically significant ($p \ll 0.01$) and adjusted R^2 values (shown on plots in blue) are similar across methods (≈ 0.3). For all methods, the differences in g-ratios between animal models is apparent, and it is clear that results from *Tsc2* mice did not follow the same linear relationship. This is demonstrated on each plot by the best-fit line and adjusted R^2 value (gray) when the *Tsc2* mice were not included in the regression. It is also noteworthy that all three DWI analyses and analysis using $f_{\mathrm{E}} = 0$ provided similar quality correspondence of g_{MRI} and g_{HIST}, suggesting the the correlations were driven primarily by the measure of f_{M}.

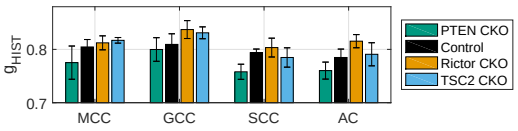

Figure 2: Mean ± standard deviation (across animals) of g_{HIST} from each ROI and mouse model

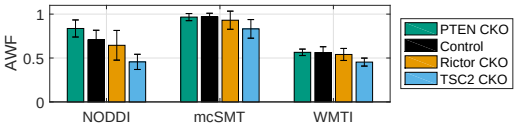

Figure 3: Mean ± standard deviation (across animals) of AWF values from each of the three DWI analyses and each mouse model

4. Discussion

Figures 4 and 5 demonstrate potential of 3D g_{MRI} mapping of ex vivo mouse brains. In general, the g_{MRI} maps are relatively smooth and show widespread amplitude variations that are consistent with histology and known white matter characteristics of these mouse models. Likewise, the g_{MRI} scatter plots show a moderate linear correspondence to g_{HIST}. However, Fig 5 also reveals shortcomings. Across all animals and methods, g_{MRI} generally overestimates g_{HIST}, especially so for the *Tsc2*. Also, in terms of g_{MRI} serving as a correlative measure of g_{HIST}, the analysis based on f_{M} maps alone (i.e., assuming $f_{\mathrm{E}} = 0$) worked approximately as well as any of the methods that used DWI-derived estimates of AWF.

The general overestimation of g_{MRI} compared to g_{HIST} may be due to a few factors. One possible source of this difference is the different definitions of the two measures. The analysis of histology did not include quantitation of non-myelinated axons, and so g_{HIST} reflects only measures of g-ratio from the myelinated axons. In contrast, to the extent that a given DWI measure of AWF includes at least some portion of non-myelinated axons, this signal will also contribute to g_{MRI}. In other words, g_{MRI} may include a weighting of $g = 1$ from some or all the non-myelinated axons and will then be greater than g_{HIST}, by definition. Another potential source of difference comes from the limitations of the DWI analysis methods. For example, the methods used here assume that extra-axonal water diffusion is Gaussian. However, with large b-values and tightly packed axons, this assumption may not be valid, which would then lead to an overestimation of axonal water fraction and, in turn, g-ratio.

These systematic inaccuracies may or may not be a problem for a particular study. For example, in comparing the control, *Rictor*, and *Pten* mice, despite the

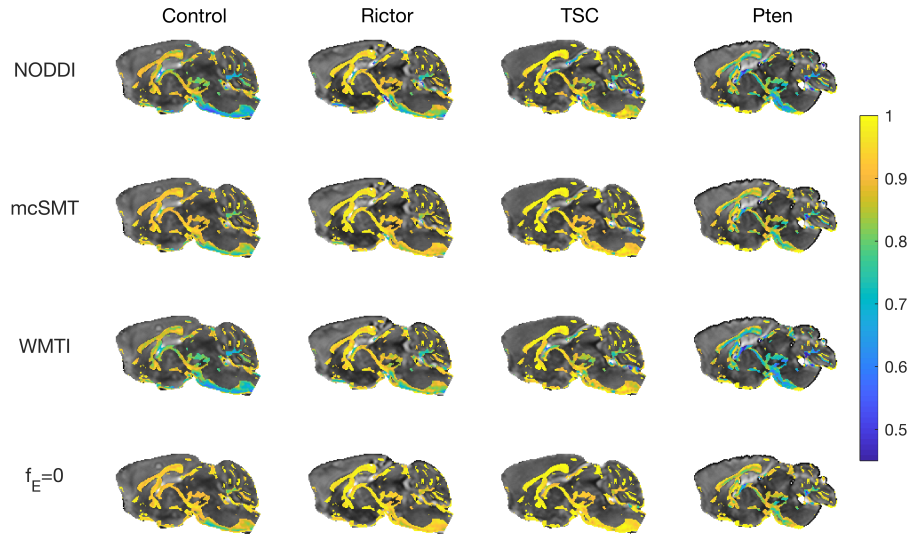

Figure 4: Representative g-ratio maps for each mouse type and DWI analysis method.

overestimation of g_{MRI} for myelinated axon g-ratio, the correlation between g_{MRI} and g_{HIST} for all analyses was moderately strong. However, this linear correlation broke down for the *Tsc2* mice. It cannot, for example, be discerned from g_{MRI} that the g-ratio values of *myelinated* axons in the *Tsc2* mice is near normal and similar to those of the *Rictor* mice.

In addition to the effect of non-myelinated axons on g_{MRI}, the data in Fig 5 also point to another systematic characteristic of g_{MRI} that may be important. Comparing g_{MRI} results across the different DWI analysis methods reveals the greatest inter-method variation for the *Pten* mice, the least for the *Tsc2* mice, and intermediate amounts for the control and *Rictor* mice. This may be surprising given that the AWF estimates themselves (Fig 3) were not especially more variant for any one mouse type, but did differ substantially between methods. The explanation, again, lies in the definition of g_{MRI}. Consider this reformulation of Eq (1),

$$g_{\mathrm{MRI}} = \sqrt{\frac{f_{\mathrm{A}}}{f_{\mathrm{A}} + f_{\mathrm{M}}}} = \sqrt{\frac{AWF(1-f_{\mathrm{M}})}{AWF(1-f_{\mathrm{M}}) + f_{\mathrm{M}}}}. \tag{4}$$

From here, it is easy to appreciate that when $f_{\mathrm{M}} \ll AWF$, $g_{\mathrm{MRI}} \to 1$ and will be relatively insensitive to the AWF value. Hence, for the *Tsc2* and *Rictor* mice ($f_{\mathrm{M}} \approx$

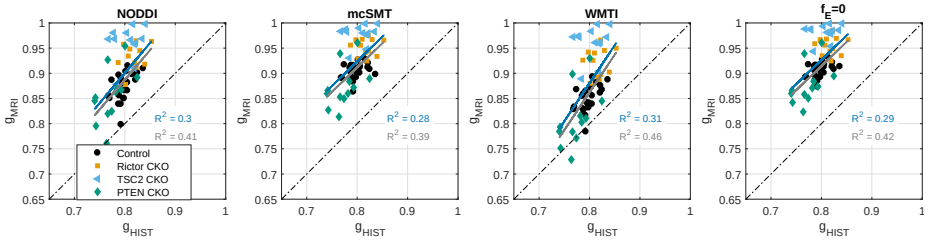

Figure 5: Scatter plots of MRI vs histological measures of g-ratio for each of the three DWI analysis protocols and analysis assuming $f_E = 0$. Shown in each frame is the best linear fit (blue), the best linear fit excluding *Tsc2* mice (gray), and the line of unity (dash-dot).

0.05 and 0.15, respectively), in particular, g_{MRI} had relatively little dependence on AWF, and for the *Pten* mice ($f_M \approx 0.25$) the effect of AWF on g_{MRI} was the greatest. This characteristic, coupled with the fact that f_M varied considerably more across mouse types than did AWF (by any DWI analysis method) also explains the g_{MRI} results obtained using the simplified model with $f_E = 0$ (right panel of Fig 5). That is, for this study, the observed correlations between g_{MRI} and g_{HIST} were driven primarily by variations in f_M between mouse types. The same situation will be true for any condition that does not include substantial changes in f_E—because AWF will also be relatively invariant, there will be little benefit in measuring it.

Although general conclusions can be drawn from the mathematical nature of the g_{MRI} model, generalizations about the data reported here should be done with caution. All of the data used in this study came from the mid-sagittal plane, where, perhaps, the dense packing of axons results in g_{MRI} or g_{HIST} values that are systematically different than in other regions. Ideally, MRI offers the potential for 3D volumetric g-ratio imaging, but comparisons to histology at arbitrary locations will be a challenge. Also, the MRI measurements were performed on excised, chemically-fixed, and contrast-enhanced samples, which introduces a number of potential variations.

The relatively low concentration of Gd (1 mM) loaded into the brains in this study is not expected to significantly alter the DWI (D'Arceuil et al., 2007) or MET_2 data (West et al., 2016b), but this has not been rigorously tested for exactly the sample preparations and MRI studies used here. For example, as discussed previously (West et al., 2016b), while f_M from MET_2 measurements works effectively in these samples, its use for human studies may be limited by scan time/signal-to-noise ratio and possibly more affected by inter-compartmental water exchange. Use of quantitative magnetization transfer (qMT) to measure f_M, which has its own challenges with regard to calibration and specificity, may offer a more efficient alternative. For comparison, supplementary Fig S2 shows the g_{MRI} vs g_{HIST} plots for the case that f_M is derived from qMT, as previously described (West et al.,

2016b). Also previously discussed (Kaden et al., 2016a), these fixed tissues exhibit relatively high residual DWI signal for gradient directions parallel to the fiber orientation, indicating the presence of slowly diffusing water that was not incorporated into any of the DWI analysis models used here. Although not shown, variations of the NODDI and mcSMT models with the addition of a stationary, or "dot", signal component (Alexander et al., 2010), were implemented as part of this study, but they did not result in stronger correlations between g_{MRI} and g_{HIST}.

It is also important to remember that g_{MRI} is an axon area-weighted measure (West et al., 2016a). Therefore, during diseases targeting either large (e.g., amyotrophic lateral sclerosis (Nguyen et al., 2000)) or small axons (e.g., the cuprizone model of demyelination (Jelescu et al., 2016; Mason et al., 2001; Thiessen et al., 2013)) or changes during development where large axons are typically myelinated first (Matthews and Duncan, 1971; Remahl and Hildebrand, 1982), the observed g_{MRI} will more heavily reflect changes in the larger axons. In addition, the g-ratio is not constant across axon size, with larger axons generally having higher g-ratios (Berthold et al., 1983); hence, if the distribution of axons in tissue changes, a different g_{MRI} may be detected.

5. Conclusion

Experimental MRI and electron microscopy studies of excised and fixed mouse brains provide the most extensive comparisons to date of g_{MRI} to histology. The results demonstrate moderate linear correlations between g_{MRI} and corresponding measures of myelinated axon g-ratio from histology (g_{HIST}), but the presence of non-myelinated axons also causes g_{MRI} to be systematically greater than g_{HIST}. Also, the observations and consideration of the model led to the conclusion that g_{MRI} reduces to be well approximated by only myelin content for cases of relatively low myelin content or any case where little variation of extra-axonal volume fraction exists.

6. Acknowledgments

We thank Dr Enrico Kaden for assistance with the mcSMT analysis and useful discussions.

7. References

References

Alexander, D. C., Hubbard, P. L., Hall, M. G., Moore, E. A., Ptito, M., Parker, G. J. M., Dyrby, T. B., Oct 2010. Orientationally invariant indices of axon diameter and density from diffusion mri. Neuroimage 52 (4), 1374–89.

Alonso-Ortiz, E., Levesque, I. R., Pike, G. B., Jan 2015. Mri-based myelin water imaging: A technical review. Magn Reson Med 73 (1), 70–81.

Arnett, H. A., Mason, J., Marino, M., Suzuki, K., Matsushima, G. K., Ting, J. P., Nov. 2001. TNF alpha promotes proliferation of oligodendrocyte progenitors and remyelination. Nature neuroscience 4 (11), 1116–1122.

Bartzokis, G., Jan 2004. Age-related myelin breakdown: a developmental model of cognitive decline and alzheimer's disease. Neurobiol Aging 25 (1), 5–18; author reply 49–62.

Beaulieu, C. F., Zhou, X., Cofer, G. P., Johnson, G. A., Aug 1993. Diffusion-weighted mr microscopy with fast spin-echo. Magn Reson Med 30 (2), 201–6.

Berman, S., Yeatman, J. D., Mezer, A., 2016. In vivo measurement of g-ratio in the corpus callosum using the macromolecular tissue volume: evaluating changes as a function of callosal subregions, age and sex. In: Toward a Super-BigBrain: Promises and Pitfalls of Microstructural Imaging. Montreal.

Berthold, C. H., Nilsson, I., Rydmark, M., May 1983. Axon diameter and myelin sheath thickness in nerve fibres of the ventral spinal root of the seventh lumbar nerve of the adult and developing cat. J Anat 136 (Pt 3), 483–508.

Campbell, J. S. W., Leppert, I. R., Narayanan, S., Boudreau, M., Duval, T., Cohen-Adad, J., Pike, G. B., Stikov, N., Aug 2017. Promise and pitfalls of g-ratio estimation with mri. Neuroimage.

Carson, R. P., Fu, C., Winzenburger, P., Ess, K. C., Jan 2013. Deletion of rictor in neural progenitor cells reveals contributions of mtorc2 signaling to tuberous sclerosis complex. Hum Mol Genet 22 (1), 140–52.

Carson, R. P., Kelm, N. D., West, K. L., Does, M. D., Fu, C., Weaver, G., McBrier, E., Parker, B., Grier, M. D., Ess, K. C., Dec 2015. Hypomyelination following deletion of tsc2 in oligodendrocyte precursors. Ann Clin Transl Neurol 2 (12), 1041–54.

Carson, R. P., Van Nielen, D. L., Winzenburger, P. A., Ess, K. C., Jan 2012. Neuronal and glia abnormalities in tsc1-deficient forebrain and partial rescue by rapamycin. Neurobiol Dis 45 (1), 369–80.

Chomiak, T., Hu, B., Nov 2009. What is the optimal value of the g-ratio for myelinated fibers in the rat cns? a theoretical approach. PLoS One 4 (11), e7754.

Daducci, A., Canales-Rodríguez, E. J., Zhang, H., Dyrby, T. B., Alexander, D. C., Thiran, J.-P., Jan 2015. Accelerated microstructure imaging via convex optimization (amico) from diffusion mri data. Neuroimage 105, 32–44.

D'Arceuil, H. E., Westmoreland, S., de Crespigny, A. J., 2007. An approach to high resolution diffusion tensor imaging in fixed primate brain. Neuroimage 35 (2), 553–565.

Dean, 3rd, D. C., O'Muircheartaigh, J., Dirks, H., Travers, B. G., Adluru, N., Alexander, A. L., Deoni, S. C. L., May 2016. Mapping an index of the myelin g-ratio in infants using magnetic resonance imaging. Neuroimage 132, 225–37.

Does, M. D., 2014.
URL http://www.vuiis.vanderbilt.edu/~doesmd/MERA/MERA_Toolbox.html

Fieremans, E., Jensen, J. H., Helpern, J. A., Sep 2011. White matter characterization with diffusional kurtosis imaging. Neuroimage 58 (1), 177–88.

Harrington, E. P., Zhao, C., Fancy, S. P. J., Kaing, S., Franklin, R. J. M., Rowitch, D. H., Nov 2010. Oligodendrocyte pten is required for myelin and axonal integrity, not remyelination. Ann Neurol 68 (5), 703–16.

Hennig, J., 1988. Multiecho imaging sequences with low refocusing flip angles. Journal of Magnetic Resonance 78 (3), 397 – 407.

Jelescu, I. O., Zurek, M., Winters, K. V., Veraart, J., Rajaratnam, A., Kim, N. S., Babb, J. S., Shepherd, T. M., Novikov, D. S., Kim, S. G., Fieremans, E., May 2016. In vivo quantification of demyelination and recovery using compartment-specific diffusion mri metrics validated by electron microscopy. Neuroimage 132, 104–14.

Jensen, J. H., Helpern, J. A., Aug 2010. Mri quantification of non-gaussian water diffusion by kurtosis analysis. NMR Biomed 23 (7), 698–710.

Jones, D. K., Horsfield, M. A., Simmons, A., Sep 1999. Optimal strategies for measuring diffusion in anisotropic systems by magnetic resonance imaging. Magn Reson Med 42 (3), 515–25.

Kaden, E., Kelm, N. D., Carson, R. P., Does, M. D., Alexander, D. C., Jun 2016a. Multi-compartment microscopic diffusion imaging. Neuroimage 139, 346–359.

Kaden, E., Kruggel, F., Alexander, D. C., Apr 2016b. Quantitative mapping of the per-axon diffusion coefficients in brain white matter. Magn Reson Med 75 (4), 1752–63.

Kelm, N. D., West, K. L., Carson, R. P., Gochberg, D. F., Ess, K. C., Does, M. D., Jan 2016. Evaluation of diffusion kurtosis imaging in ex vivo hypomyelinated mouse brains. Neuroimage 124 (Pt A), 612–26.

Lassmann, H., 2004. Cellular Damage and Repair in Multiple Sclerosis. In: Lazzarini, R. A. (Ed.), Myelin Biology and Disorders. Elsevier, London, pp. 733–762.

Laule, C., Leung, E., Lis, D. K. B., Traboulsee, A. L., Paty, D. W., MacKay, A. L., Moore, G. R. W., Dec 2006. Myelin water imaging in multiple sclerosis: quantitative correlations with histopathology. Mult Scler 12 (6), 747–53.

Laule, C., Vavasour, I. M., Kolind, S. H., Li, D. K. B., Traboulsee, T. L., Moore, G. R. W., MacKay, A. L., Jul 2007. Magnetic resonance imaging of myelin. Neurotherapeutics 4 (3), 460–84.

Mancini, M., Giulietti, G., Dowell, N., Spanò, B., Harrison, N., Bozzali, M., Cercignani, M., Sep 2017. Introducing axonal myelination in connectomics: A preliminary analysis of g-ratio distribution in healthy subjects. Neuroimage.

Mason, J. L., Langaman, C., Morell, P., Suzuki, K., Matsushima, G. K., Feb 2001. Episodic demyelination and subsequent remyelination within the murine central nervous system: changes in axonal calibre. Neuropathol Appl Neurobiol 27 (1), 50–8.

Matthews, M. A., Duncan, D., May 1971. A quantitative study of morphological changes accompanying the initiation and progress of myelin production in the dorsal funiculus of the rat spinal cord. J Comp Neurol 142 (1), 1–22.

Menzies, L., Chamberlain, S. R., Laird, A. R., Thelen, S. M., Sahakian, B. J., Bullmore, E. T., 2008. Integrating evidence from neuroimaging and neuropsychological studies of obsessive-compulsive disorder: the orbitofronto-striatal model revisited. Neurosci Biobehav Rev 32 (3), 525–49.

Mighdoll, M. I., Tao, R., Kleinman, J. E., Hyde, T. M., Jan 2015. Myelin, myelin-related disorders, and psychosis. Schizophr Res 161 (1), 85–93.

Mohammadi, S., Carey, D., Dick, F., Diedrichsen, J., Sereno, M. I., Reisert, M., Callaghan, M. F., Weiskopf, N., 2015. Whole-brain in-vivo measurements of the axonal g-ratio in a group of 37 healthy volunteers. Front Neurosci 9, 441.

Nguyen, M. D., Larivière, R. C., Julien, J. P., Oct 2000. Reduction of axonal caliber does not alleviate motor neuron disease caused by mutant superoxide dismutase 1. Proc Natl Acad Sci U S A 97 (22), 12306–11.

Prasloski, T., Mädler, B., Xiang, Q.-S., MacKay, A., Jones, C., Jun 2012. Applications of stimulated echo correction to multicomponent t2 analysis. Magn Reson Med 67 (6), 1803–14.

Remahl, S., Hildebrand, C., Apr 1982. Changing relation between onset of myelination and axon diameter range in developing feline white matter. J Neurol Sci 54 (1), 33–45.

Rushton, W. A. H., Sep 1951. A theory of the effects of fibre size in medullated nerve. J Physiol 115 (1), 101–22.

Stikov, N., Campbell, J. S. W., Stroh, T., Lavelée, M., Frey, S., Novek, J., Nuara, S., Ho, M.-K., Bedell,

B. J., Dougherty, R. F., Leppert, I. R., Boudreau, M., Narayanan, S., Duval, T., Cohen-Adad, J., Picard, P.-A., Gasecka, A., Côté, D., Pike, G. B., Sep 2015. In vivo histology of the myelin g-ratio with magnetic resonance imaging. Neuroimage 118, 397–405.

Stikov, N., Perry, L. M., Mezer, A., Rykhlevskaia, E., Wandell, B. A., Pauly, J. M., Dougherty, R. F., Jan 2011. Bound pool fractions complement diffusion measures to describe white matter micro and macrostructure. Neuroimage 54 (2), 1112–21.

Tabesh, A., Jensen, J. H., Ardekani, B. A., Helpern, J. A., Mar 2011. Estimation of tensors and tensor-derived measures in diffusional kurtosis imaging. Magn Reson Med 65 (3), 823–36.

Thiessen, J. D., Zhang, Y., Zhang, H., Wang, L., Buist, R., Del Bigio, M. R., Kong, J., Li, X.-M., Martin, M., Nov 2013. Quantitative mri and ultrastructural examination of the cuprizone mouse model of demyelination. NMR Biomed 26 (11), 1562–81.

Thirion, J. P., Sep 1998. Image matching as a diffusion process: an analogy with maxwell's demons. Med Image Anal 2 (3), 243–60.

Weinstein, M., Ben-Sira, L., Levy, Y., Zachor, D. A., Ben Itzhak, E., Artzi, M., Tarrasch, R., Eksteine, P. M., Hendler, T., Ben Bashat, D., Apr 2011. Abnormal white matter integrity in young children with autism. Hum Brain Mapp 32 (4), 534–43.

West, K. L., Kelm, N. D., Carson, R. P., Does, M. D., Jan 2016a. A revised model for estimating g-ratio from mri. Neuroimage 125, 1155–8.

West, K. L., Kelm, N. D., Carson, R. P., Gochberg, D. F., Ess, K. C., Does, M. D., Dec 2016b. Myelin volume fraction imaging with mri. Neuroimage.

Whittall, K., MacKay, A., 1989. Quantitative interpretation of nmr relaxation data. Journal of Magnetic Resonance (1969) 84 (1), 134–152.

Zhang, H., Schneider, T., Wheeler-Kingshott, C. A., Alexander, D. C., Jul 2012. Noddi: practical in vivo neurite orientation dispersion and density imaging of the human brain. Neuroimage 61 (4), 1000–16.